

Gate-Tunable Kinetic Inductance in Proximitized Nanowires

Lukas Johannes Splitthoff^{1,2,*}, Arno Bargerbos^{1,2}, Lukas Grünhaupt^{1,2}, Marta Pita-Vidal^{1,2},
Jaap Joachim Wesdorp^{1,2}, Yu Liu³, Angela Kou⁴, Christian Kraglund Andersen^{1,2} and
Bernard van Heck⁵


¹*QuTech, Delft University of Technology, Delft 2628 CJ, Netherlands*

²*Kavli Institute for Nanoscience, Delft University of Technology, Delft 2628 CJ, Netherlands*

³*Center for Quantum Devices, Niels Bohr Institute, University of Copenhagen, Copenhagen 2100, Denmark*

⁴*Department of Physics and Frederick Seitz Materials Research Laboratory, University of Illinois Urbana-Champaign, Urbana, Illinois 61801, USA*

⁵*Leiden Institute of Physics, Leiden University, 2333 CA Leiden, Netherlands*

 (Received 8 March 2022; revised 22 June 2022; accepted 1 July 2022; published 29 August 2022)

We report the detection of a gate-tunable kinetic inductance in a hybrid InAs/Al nanowire. For this purpose, we embed the nanowire into a quarter-wave coplanar waveguide resonator and measure the resonance frequency of the circuit. We find that the resonance frequency can be changed via the gate voltage that controls the electron density of the proximitized semiconductor and thus the nanowire inductance. Applying Mattis-Bardeen theory, we extract the gate dependence of the normal-state conductivity of the nanowire, as well as its superconducting gap. Our measurements complement existing characterization methods for hybrid nanowires and provide a useful tool for gate-controlled superconducting electronics.

DOI: [10.1103/PhysRevApplied.18.024074](https://doi.org/10.1103/PhysRevApplied.18.024074)

I. INTRODUCTION

Superconducting wires with high kinetic inductance [1–8] have found useful applications as radiation detectors [9] and, more recently, in the field of quantum technology [10–12], where they are particularly beneficial for protected superconducting qubit designs [13–18].

Typically, the kinetic inductance of a nanofabricated sample is determined by the material composition and by the device geometry and, thus, is not tunable *in situ*. Yet, some applications rely critically on the ability to tune the inductor of a quantum circuit after fabrication, e.g., for superconducting amplifiers [19–21]. Such tunability has commonly been achieved through the use of flux-biased dc superconducting quantum interference devices (SQUIDs) [22,23] or current-biased conductors [2,19,21,24–26].

A more recent source of tunability comes from the advent of hybrid semiconducting-superconducting nanostructures, which allow the realization of gate-tunable Josephson junctions [27–29]. Even a semiconducting nanowire proximitized by a continuous superconducting film, without any Josephson junction, can be controlled electrostatically. Nearby gates influence the electron density in the semiconductor as well as the induced superconducting gap [30–33], the two crucial parameters, which control the inductive response. This electrostatic control

over the properties of the proximitized nanowire suggests the possibility to realize a gate-tunable kinetic inductance by exploiting the proximitized transport channels. Such a circuit element could allow for an additional class of frequency-controllable resonators, amplifiers, qubits, and detectors.

Here, we experimentally demonstrate a gate-tunable kinetic inductance using an InAs/Al nanowire shunting a Nb_xTi_{1-x}N coplanar waveguide (CPW) resonator. This system offers an easy-to-fabricate and magnetic-field-compatible [34,35] circuit element for superconducting electronics. Furthermore, facilitated by the absence of etched Al segments in the nanowire, we are able to extract bulk transport properties of the hybrid InAs/Al system, which has recently attracted lots of attention for its potential use in topologically protected qubits [36].

II. EXPERIMENTAL SETUP

We employ a quarter-wave coplanar waveguide resonator, which is capacitively coupled to a feedline and shorted to ground by the proximitized nanowire, see Fig. 1(a). The $l = 3 \mu\text{m}$ long nanowire section is galvanically connected to the central conductor of the resonator and to the ground, see Fig. 1(c). The nanowire is encapsulated by bottom and top gates for electrostatic control. In this experiment we use the bottom gate only, which extends along the entire nanowire section (optically hidden by the top gate), as illustrated in Fig. 1(d). Each gate line is filtered by

*L.J.Splitthoff@tudelft.nl

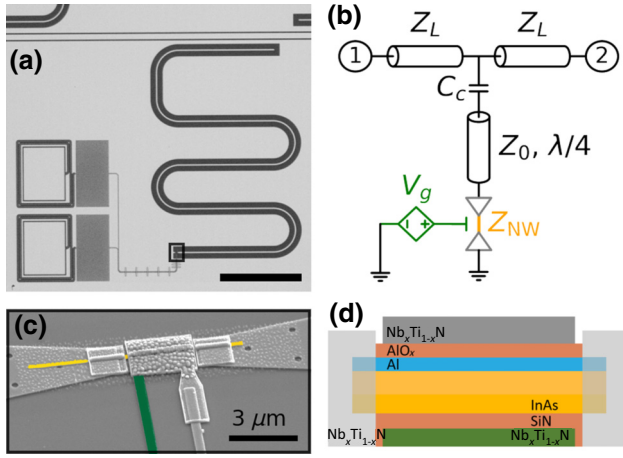


FIG. 1. Measured device and equivalent circuit. (a) Optical image of one quarter-wave coplanar waveguide resonator capacitively coupled to a feedline and shorted to the ground via a proximitized nanowire. Two LC filtered pads left to the resonator connect to the gates in the vicinity of the nanowire. (scale bar $300\ \mu\text{m}$). (b) Circuit diagram of a measured device. The transmission line resonator with impedance Z_0 is shunted to the ground by a hybrid nanowire with impedance Z_{NW} , which is voltage gate controlled (V_g), and capacitively coupled (C_C) to the feedline with characteristic impedance $Z_L = 50\ \Omega$. Ports 1 and 2 connect to the external measurement setup. (c) False colored micrograph of a proximitized nanowire (orange), which is galvanically connected to the central conductor of the resonator [black box in (a)]. The $3\text{-}\mu\text{m}$ -long nanowire section is encapsulated by bottom (green) and top (grey) gates. For this experiment we only use the bottom gate. (d) Schematic longitudinal cut away of InAs nanowire (yellow) with continuous Al shell (blue) between two $\text{Nb}_x\text{Ti}_{1-x}\text{N}$ contacts. Bottom (green) and top (gray) gates with dielectric (orange) define the electrostatic potential at the nanowire.

on-chip LC filters [37]. The schematic longitudinal cross section in Fig. 1(d) highlights the continuous Al shell on two facets of the gated InAs nanowire, which is connected to the $\text{Nb}_x\text{Ti}_{1-x}\text{N}$ circuit (Appendix A).

To characterize the bare resonator properties, we use an identical reference resonator, in which the nanowire is replaced by a continuous 150-nm -thick $\text{Nb}_x\text{Ti}_{1-x}\text{N}$ film (Appendix E 2). Multiple nanowire and reference resonators are frequency multiplexed on the same chip and measured at 15-mK base temperature inside a dilution refrigerator. In the main text, we focus on one nanowire [two-facet Al-InAs nanowire, $(110 \pm 5)\text{-nm}$ diameter, 6-nm -thick Al shell], and one reference resonator, which exemplify trends observed in 12 different devices (Appendix E 1).

III. GATE-TUNABLE KINETIC INDUCTANCE

The nanowire resonator system can be described by the circuit model in Fig. 1(b): a transmission line with

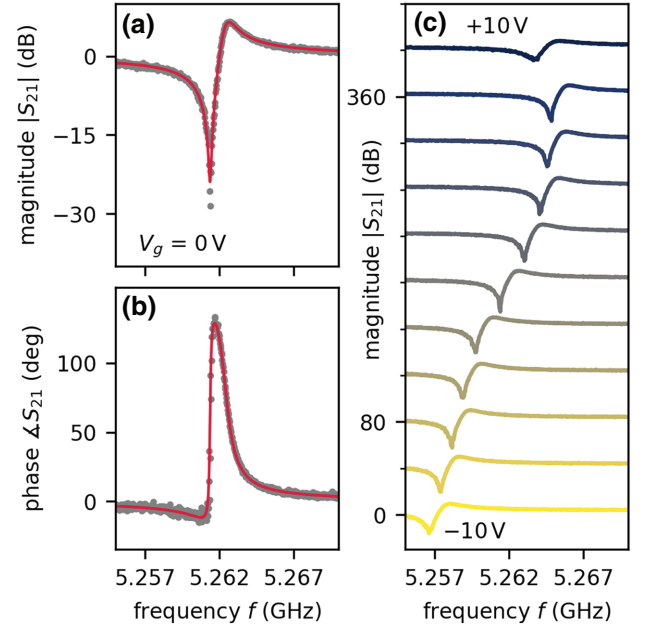


FIG. 2. Gate-dependent frequency shift of the nanowire resonator. (a),(b) Typical magnitude and phase of transmission parameter S_{21} , respectively, of a single nanowire resonator for a fixed gate voltage $V_0 = 0\ \text{V}$. Red line shows fit result. (c) Magnitude of the transmission S_{21} for 11 different, linear spaced gate voltages in the range from -10 to $10\ \text{V}$. Each line with a fixed gate voltage is offset by $40\ \text{dB}$ for better visibility.

characteristic impedance Z_0 is shunted by a gate-voltage-dependent (V_g) impedance Z_{NW} , and capacitively coupled (C_C) to a common feedline ($Z_L = 50\ \Omega$). We measure the transmission parameter S_{21} in the vicinity of the resonance frequency. The amplitude and phase of S_{21} display typical resonant behavior, as shown in Figs. 2(a) and 2(b). We use a linear resonator model [38,39] to fit the resonance frequency f_r and internal quality factor Q_i .

We observe a monotonic increase in resonance frequency as a function of gate voltage up to $8\ \text{V}$ [Fig. 2(c)]. The shift is about $8\ \text{MHz}$ over the total gate range available for measurement (-10 to $10\ \text{V}$). In Figs. 3(a) and 3(b), we show the extraction of f_r and Q_i as a function of gate voltage. The internal quality factor is nearly constant in the entire range, but it decreases sharply at large applied voltages, an effect that we attribute to the breakdown of the gate dielectric (Appendix E 5).

When the temperature is increased, the resonance frequency and internal quality factor decrease, at all gate voltages, see Figs. 3(c) and 3(d). We attribute this behavior to the suppression of superconductivity in Al. Between 20 and $750\ \text{mK}$, the frequency is reduced by about $6\ \text{MHz}$, while Q_i drops by one order of magnitude. We notice that for both quantities the temperature response exhibits a gate dependence: it is stronger for positive gate voltages, which, as shown below, we attribute to a change in the induced

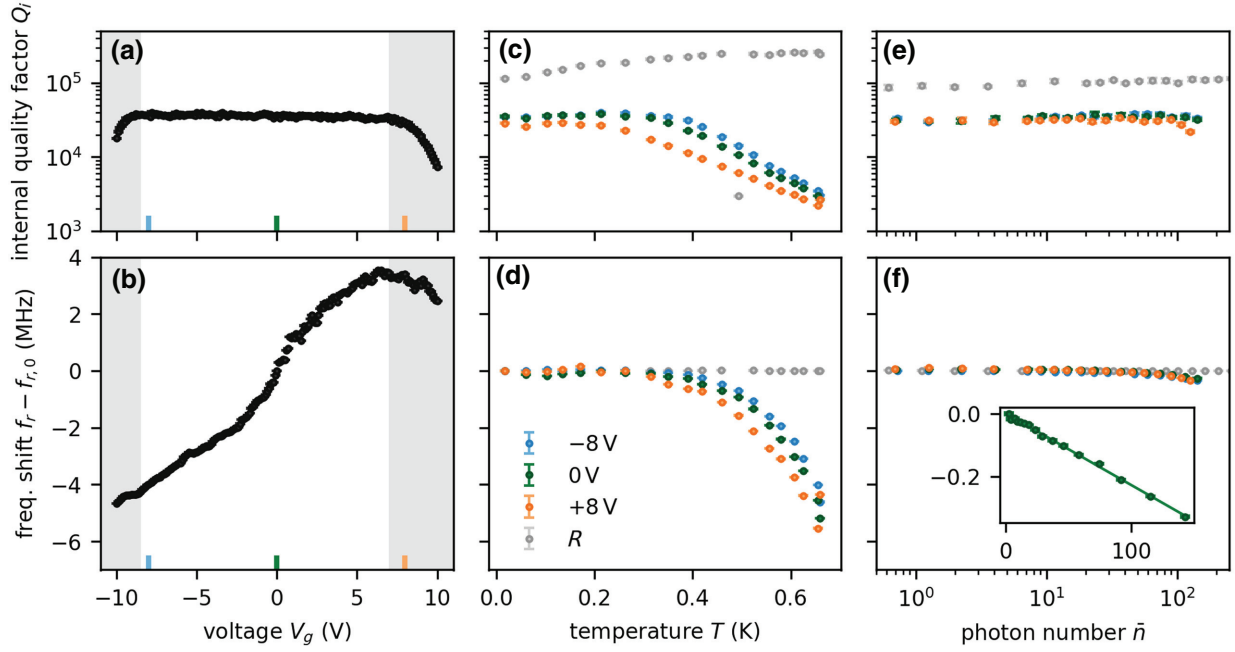


FIG. 3. Resonator response versus control parameters. (a),(b) Internal quality factor and frequency shift as a function of gate voltages extracted from fits to S_{21} data [cf. Figs. 2(a) and 2(b)]. The gray boxes indicate the regions of decreasing Q_i for $V_g < -8.5$ V and $V_g > 7$ V (see main text). Colored lines at the bottom mark gate points used in (c)–(f). (c),(d) Internal quality factor and frequency shift for the nanowire resonator versus temperature for different gate voltages relative to their zero temperature values. Reference resonator (R) data shown for comparison. (e),(f) Internal quality factor and frequency shift for the nanowire resonator versus average intracavity photon number for different gate voltages. For higher photon number, the nanowire resonator becomes increasingly nonlinear and the linear fit model does not capture the measured data above $\bar{n} \gtrsim 200$. Reference resonator (R) data shown for comparison. The error bars indicate the 1σ confidence interval of fit. Inset: enlargement of the frequency shift of the nanowire resonator at 0 V with linear fit.

superconducting gap in InAs. In contrast, in the same temperature range, the resonance frequency of the reference resonator remains approximately constant, while Q_i increases slightly. These observations are consistent with the much higher critical temperature of $\text{Nb}_x\text{Ti}_{1-x}\text{N}$ and the saturation of two-level systems contributing to dielectric losses [40].

The resonance frequency decreases linearly with the number of intracavity photons, \bar{n} , as expected in the presence of a Kerr nonlinearity arising from the inductance [41,42]. The frequency shift relative to the single-photon level (Appendix B) is about 0.2 MHz at -120 dBm input power, corresponding to $\bar{n} \approx 100$ [Figs. 3(e) and 3(f)], one order of magnitude smaller than the frequency shifts observed versus gate voltage or temperature. We measure a Kerr coefficient $K/2\pi = (f_r - f_{r,0})/\bar{n} = (2.28 \pm 0.03)$ kHz [inset Fig. 3(f)], which is sufficient for the realization of superconducting parametric amplifiers [41,43]. For larger photon numbers, higher-order nonlinear processes set in and the resonator bifurcates [44,45], thus the linear model does not capture the measured data for $\bar{n} \gtrsim 200$ (Appendix E 4). The reference resonator inductance is not susceptible to these photon numbers, thus there is no frequency shift. Q_i increases with microwave power, which is consistent with the saturation of two-level

systems [40]. We thus choose 100 intracavity photons for the remaining measurements to have sufficient signal-to-noise ratio without inducing strong nonlinear effects on the nanowire.

IV. BULK PROPERTIES OF THE PROXIMITIZED NANOWIRE

We use the measured frequency shifts to extract relevant physical properties of the hybrid nanowire. Assuming that the imaginary part of the nanowire impedance is purely inductive, $\text{Im}(Z_{\text{NW}}) = 2\pi f_{\text{NW}}L_{\text{NW}}$, which is justified given the electromagnetic field profile along the resonator in the limit $Z_{\text{NW}} \ll Z_0$, a loaded transmission-line resonator model (Appendix D) yields the nanowire inductance $L_{\text{NW}} = Z_0/4(f_{\text{NW}}^{-1} - f_0^{-1})$, where f_{NW} is the resonance frequency of the loaded nanowire resonator and Z_0 and f_0 are the characteristic impedance and resonance frequency of the unloaded coplanar waveguide resonator. Using a conformal mapping technique [46] and the average kinetic sheet inductance of the $\text{Nb}_x\text{Ti}_{1-x}\text{N}$ film obtained from the measurement of four reference resonators, we determine $Z_0 = (134.2 \pm 0.4) \Omega$ and $f_0 = (5.502 \pm 0.016)$ GHz. The uncertainties of these quantities mainly depend on the uncertainty of the $\text{Nb}_x\text{Ti}_{1-x}\text{N}$

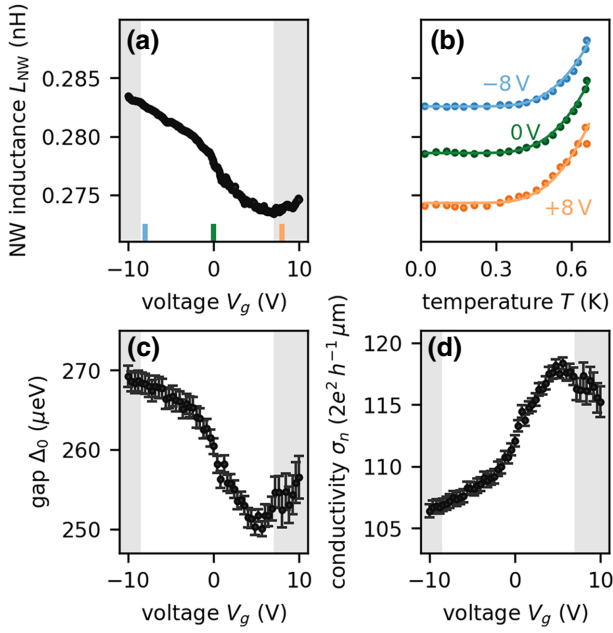


FIG. 4. Extracted nanowire parameters from resonator data shown in Fig. 3. (a) Inductance of the nanowire resonator versus gate voltage extracted from loaded resonator model (see main text). (b) Nanowire resonator inductance versus temperature for three different gate voltages. Lines indicate fit to the Mattis-Bardeen model. (c) Superconducting gap Δ_0 extracted from the fit to the temperature dependence for each gate voltage. (d) Normal-state conductivity σ_n extracted from the fit to the temperature dependence for each gate voltage. The grayed-out areas indicate the regions of decreasing Q_i .

kinetic sheet inductance. Thus, we can extract L_{NW} from the measured f_{NW} , as shown in Fig. 4(a).

At zero voltage, the nanowire inductance is $L_{NW} = (278 \pm 17)$ pH with about 6% constant systematic error stemming from the uncertainties on Z_0 and f_0 . L_{NW} varies by 3.5% over the range from -10 to 7 V before superconductivity is suppressed by gate leakage. The geometric inductance associated with the nanowire segment can be estimated to be $L_{NW,geo} = 4.5$ pH (Appendix E 3), thus we conclude that the shunt impedance is dominated by the kinetic inductance of the hybrid nanowire.

Using the same method, we extract the temperature dependence of L_{NW} , as shown in Fig. 4(b). For all gate voltages, the nanowire inductance increases with temperature. According to the Mattis-Bardeen theory [47,48] in the low-frequency limit, $hf \ll \Delta_0$, the kinetic inductance is given by

$$L_{NW} = \frac{\hbar l}{\pi \sigma_n \Delta_0} \tanh^{-1} \left(\frac{\Delta_0}{2k_B T} \right), \quad (1)$$

where Δ_0 is the superconducting gap and σ_n is the one-dimensional normal-state conductivity of the hybrid nanowire. Note that the latter absorbs the cross-section

electron density distribution and has physical dimensions of conductance times length. The increase of L_{NW} with temperature can be used to extract Δ_0 as a function of gate voltage.

Increasing the gate voltage, the extracted superconducting gap decreases by 7% from (270 ± 1) μeV to (251 ± 1) μeV [Fig. 4(c)]. We note that at higher temperature, the onset of gate leakage shifts down to 5 V causing an increase in the fit uncertainty and interrupting the monotonous decrease of the gap with gate voltage. Moreover, we observe two distinct slopes: a shallow slope between -10 and -2 V and a steeper slope between -2 and 5 V. Similar observations have also been made in previous experiments on similar devices [30–33,49]. We attribute the first regime to the strong hybridization of the InAs sub-bands with Al, and the second to an increase in the density in InAs with the occupation of additional sub-bands. We do not observe a plateau in the bulk properties at negative gate voltages, which indicates that we have not reached the full depletion of the semiconductor. Whether the latter is possible at all depends on the value of the band-offset pinning the conduction band of InAs at the InAs/Al interface. If the band offset is too large, it may not be possible to reach full depletion by decreasing the gate voltage further, since eventually the gate may be screened by the accumulation of holes on the facets of the InAs nanowire closer to the gate electrode [31]. We note that even over this large gate voltage range, the extracted gap remains finite. This observation does not rule out the possible onset, at positive gate voltages, of unproximitized states on the opposite side of Al-covered nanowire facets [33]. These states, if present, would not contribute considerably to the kinetic inductance.

Having determined the gate dependence of Δ_0 , we can use Eq. (1) to extract σ_n using the values of L_{NW} measured at the lowest temperature [Fig. 4(d)]. The resulting normal-state conductivity increases by 10% over the gate-voltage range. This change in conductivity translates, for a nanowire length of $3 \mu\text{m}$, to an increase in conductance of approximately $3.9 2e^2 h^{-1}$, giving a lower bound of four proximitized conduction channels added under the Al shell. Our measurement also yields a normal-state resistance at -10 V of $R_n = (365 \pm 1) \Omega$ or $R_{\square} = (13.4 \pm 0.1) \Omega \square^{-1}$, which is consistent with the expected values for a $3\text{-}\mu\text{m}$ -long and 110-nm -wide Al thin film [50]. The increase of conductivity with gate voltage overcompensates the simultaneous decrease of Δ_0 to determine the decrease of the inductance L_{NW} with gate voltage.

We note that the Mattis-Bardeen theory is formulated for a simple BCS superconductor and thus it does not capture the fact that the induced gap in the semiconductor could be different from that in the Al shell [51], and possibly varies among the proximitized subbands [31,32,52–54]. While these differences may cause strong deviations from the Mattis-Bardeen theory regarding the microwave

absorption spectrum at frequencies comparable to the gap, the low-frequency inductive response of the condensate is likely to be less sensitive to the precise profile of the density of states. As a straightforward ansatz, it is therefore sensible to test the applicability of Eq. (1) to the data. *A posteriori*, the results reveal gate-voltage trends that are consistent with those expected from detailed microscopic modeling of the field effect in the InAs/Al system [51, 54, 55], thus validating this simple approach. However, in order to fit the gate dependence of the data to microscopic parameters such as the hybridization strength between the two materials, an extension of the Mattis-Bardeen theory to proximitized systems would be required.

V. CONCLUSIONS

This experiment complements existing characterization methods for hybrid nanowires, which have been primarily based on low-frequency transport techniques [56–59]. The measurement of the microwave kinetic inductance allows us to directly probe the bulk properties of the hybrid nanowires, in contrast with measurement on devices with etched Josephson junctions, which are affected by the junction geometry and fabrication details. Given that the kinetic inductance gives access to the normal-state conductivity in the proximitized nanowire, our method, if complemented with a capacitive measurement of the electron density via the bottom gate [60], could allow extraction of the mobility of the semiconductor under the Al shell. Such a measurement could be of relevance to determine whether the hybrid system meets the stringent disorder requirements for Majorana applications [61]. The value of resonator-based material characterization in the context of hybrid systems has recently been demonstrated in 2DEGs [50].

Besides the fundamental interest to characterize hybrid nanowires, the presented approach offers a promising path towards gate-controlled superconducting electronics. In particular, the low-loss and finite Kerr nonlinearity will allow for frequency-tunable resonators, switches, microwave detectors, and parametric amplifiers [62]. In view of the potential application as frequency tunable resonators we report the frequency stability and hysteresis in Appendix E 6. The tunable frequency range can be enhanced by optimizing the choice of materials (e.g., including dielectrics with larger dielectric constants), the design of the gate electrodes, and the participation ratio of the nanowire inductance to the total resonator inductance.

The raw data and the data-analysis code at the basis of the results presented in this work are available online [63].

ACKNOWLEDGMENTS

We thank Peter Krogstrup for the supervision of the material growth and Leo P. Kouwenhoven for support and discussion. We also thank Andrey Antipov and Andrew

Higginbotham for their careful feedback on the paper. This research was co-funded by the allowance for Top consortia for Knowledge and Innovation (TKI) from the Dutch Ministry of Economic Affairs and the Microsoft Quantum initiative. C.K.A. and B.v.H. acknowledge financial support from the Dutch Research Council (NWO). L.J.S., B.v.H., and A.K. conceived the experiment. L.J.S. fabricated the devices with help from M.P.V. Nanowires were grown by Y.L. L.J.S. acquired and analyzed the data with input from A.B., L.G., A.K., C.K.A., and B.v.H. L.J.S., C.K.A., and B.v.H. wrote the paper with input from all other co-authors. A.K., C.K.A., and B.v.H. supervised the project.

APPENDIX A: FABRICATION

We fabricate the resonator circuit and the gate lines from a 35-nm-thick sputtered $\text{Nb}_x\text{Ti}_{1-x}\text{N}$ film on low-pressure chemical vapor deposition (LPCVD) SiN on Si. The kinetic sheet inductance of $(5.31 \pm 0.05) \text{ pH } \square^{-1}$ is measured using four reference resonators multiplexed to the same feedline, see Sec. E 2. We pattern the ground plane using e-beam lithography and SF_6/O_2 based reactive ion etching. 30-nm-thick plasma-enhanced chemical vapour deposition (PECVD) SiN serves as bottom gate dielectric. We transfer the two-facet InAs/Al nanowire on top of the SiN bottom gate with a nanomanipulator. The InAs nanowires are grown by vapor-liquid-solid (VLS) growth with a diameter of $(110 \pm 5) \text{ nm}$, and nominal thickness of the Al of 6 nm [64]. We electrically contact the nanowires to the circuit via lift-off defined 150-nm-thick sputtered $\text{Nb}_x\text{Ti}_{1-x}\text{N}$ leads after Ar milling, which reduces the contact resistance. Similarly, we add top gates made from AlOx dielectrics and $\text{Nb}_x\text{Ti}_{1-x}\text{N}$ to the design to overcome a possible lack of tunability due to the uncontrolled alignment of the Al shell with respect to the gates, but do not use them in this experiment as they got shorted to ground in a subsequent fabrication step. The grains visible in the SEM of the nanowire segment in the main text originate from polymer resist residuals.

APPENDIX B: MEASUREMENT SETUP

For the microwave spectroscopy, we use a rf transmission measurement setup installed in a dilution refrigerator operating at 15-mK base temperature, see Fig. 5. We probe the sample with resonators using a vector network analyser (VNA). The input line consists of microwave attenuators at room temperature (-20 dB) and at cryogenic temperatures (-70 dB). In addition, at each of the four temperature stages eccosorb filters with about 0.85-dB attenuation per 10 GHz are installed. The cables connecting the VNA to the 4-K plate add about 8 dB of attenuation. Then, NbTi cables connect to the 15-mK plate. We estimate the total input attenuation up to the sample plane to be (-105 ± 5)

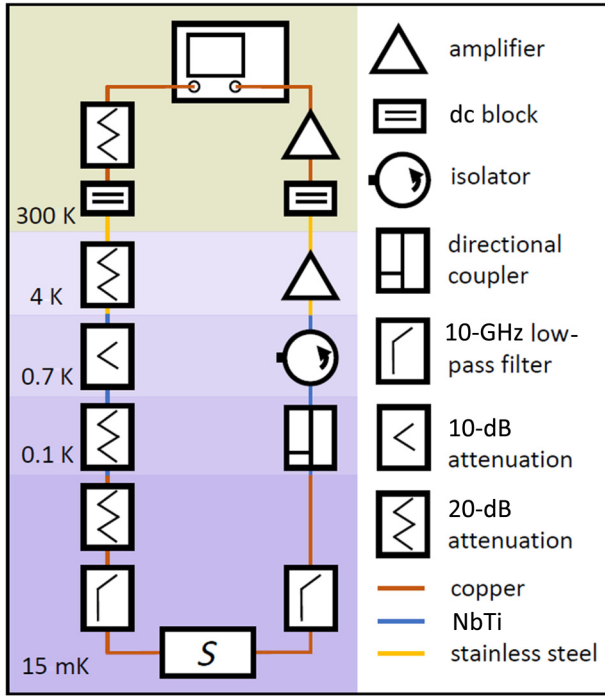


FIG. 5. Transmission measurement setup. A vector network analyzer connected to highly attenuated input and amplified output line probes the sample (S) with resonators.

dB when accounting for the additional insertion loss of filters and other cable connections to the sample mount. The 5-dB uncertainty arises from the summation of the individual components measured at room temperature. Based on this attenuation we compute the intraresonator photon number [40]

$$\bar{n} = \frac{2Q_t^2}{2\pi f_r Q_c} \frac{P_{\text{in}}}{hf_r}, \quad (\text{B1})$$

where Q_t is the total quality factor, Q_c is the coupling quality factor, and P_{in} is the power at the input port of the sample. The intraresonator photon number deviates from the true value by not more than a factor of 3.2 due to the uncertainty of the input attenuation.

The 2×7 mm chip on which the measurements are performed is glued with silver paint onto a gold-plated copper mount and electrically connected to a printed circuit board using aluminium wire bonds.

The output signal is amplified using a high electron mobility transistor amplifier at the 4-K stage. An isolator with 42-dB typical isolation prevents reflections. The directional coupler in the output line couples to an unused microwave line. The 10-GHz low-pass filter at both input and output lines clean up the spectrum. dc blocks are placed at the breakout point of the fridge. A room-temperature amplifier amplifies the signal before it enters the receiver port of the VNA.

The electrostatic gates are controlled via dc lines using a QuTech IVVI rack. The dc lines are low-pass filtered at the mixing chamber stage.

APPENDIX C: RESONATOR FITTING

We use a background-corrected linear notch-type resonator model [65] to fit the acquired resonator data. The model is based on the scattering parameter of the resonator

$$S_{21} = 1 - \frac{Q_c^{-1}(1 + ia)}{Q_c^{-1} + Q_i^{-1} + 2idf}, \quad (\text{C1})$$

where $df = f/f_r - 1$ is the frequency ratio, a is the asymmetry arising from the complex loading of the resonator, Q_c is the coupling quality factor, and Q_i is the internal quality factor [38,39]. We correct the scattering parameter of the resonator by multiplying a general background model to S_{21} and obtain the system scattering parameter

$$\tilde{S}_{21} = (m_0 + m_1 f) e^{2\pi i f \tau + i\varphi} S_{21}, \quad (\text{C2})$$

which we fit to the data. The background model includes a linear magnitude with offset m_0 and slope m_1 and a linear phase with offset φ and slope τ .

APPENDIX D: EXTRACTION OF NANOWIRE IMPEDANCE

We employ a loaded transmission-line resonator model [66] to extract the impedance of the nanowire Z_{NW} from the measurement of the resonant frequency ω_{NW} and internal quality factor Q_i of the nanowire resonator. The input impedance of a transmission line of length l_0 loaded by an impedance Z_{NW} can be written as

$$Z_{\text{in}} = Z_0 \frac{Z_{\text{NW}} + Z_0 \tanh(\alpha_0 l_0 + i\beta l_0)}{Z_0 + Z_{\text{NW}} \tanh(\alpha_0 l_0 + i\beta l_0)}. \quad (\text{D1})$$

Here, Z_0 is the frequency-dependent characteristic impedance of the transmission line, α_0 is the absorption coefficient, and β is the frequency-dependent propagation coefficient. The use of Eq. (D1) is justified for our devices since the length of the nanowire is much shorter than that of the resonator.

We are interested in the input impedance close to the fundamental frequency of the nanowire resonator. In the limit of a small nanowire impedance, this frequency will be close to the fundamental frequency of the unloaded resonator, ω_0 , which can be measured via the reference resonators, as discussed in the main text. We therefore expand Eq. (D1) close to this frequency. Furthermore, we assume that the intrinsic losses are small, $\alpha_0 l_0 \ll 1$, thus the characteristic impedance reduces to $Z_0 = \sqrt{L/C}$, where L is the series inductance and C is the shunt capacitance per unit

TABLE I. Overview of nanowire resonator parameters. In this paper we focus on the nanowire resonator denoted S11 N2. The designed width w , spacing s , and length l of the CPW resonator as well as the kinetic sheet inductance per square of the $\text{Nb}_x\text{Ti}_{1-x}\text{N}$ film L_k , the extracted inductance of the nanowire at 0 V, the measured resonance frequency at 0 V, the voltage range ΔV_g , the maximal change in frequency Δf_{NW} , and the maximal change in inductance ΔL_{NW} are given.

Label	w μm	s μm	l μm	L_k $\text{pH}\square^{-1}$	L_{NW} nH	f_{NW} GHz	ΔV_g V	Δf_{NW} MHz	ΔL_{NW} pH
S04 N1	5	20	4898	5.50	0.45	3.629	10	5.9	15
S06 N2	5	20	4948	5.67	0.31	3.617	15	8.2	22
S07 N1	4	20	3200	5.45	0.62	5.087	16	3.2	5
S09 N1	5	20	3700	7.30	0.23	4.483	16	1.1	2
S09 N2	5	20	3290	7.30	0.31	4.973	16	1.4	2
S09 N3	5	20	2950	7.30	1.18	4.883	16	19.2	30
S09 N4	5	20	2650	7.30	0.37	6.046	16	1.3	1
S10 N1	5	20	3700	7.30	0.27	4.459	19	1.9	4
S10 N2	5	20	3290	7.30	0.30	4.978	19	2.2	3
S11 N2	5	20	3430	5.31	0.28	5.262	20	8.2	10
S11 N3	5	20	3030	5.31	0.33	5.873	20	14.9	15
S11 N4	5	20	2713	5.31	0.22	6.654	20	13.8	11

length of the transmission line. In the limit $|Z_{\text{NW}}| \ll Z_0$ we obtain

$$Z_{\text{in}} \approx \frac{2\omega_0 Z_0}{\pi} \frac{1}{\frac{1}{2}\Gamma + i(\omega - \omega_{\text{NW}})}, \quad (\text{D2})$$

where ω_{NW} is the shifted resonant frequency of the nanowire resonator,

$$\omega_{\text{NW}} = \omega_0 \left[1 - \frac{2 \text{Im}(Z_{\text{NW}})}{\pi Z_0} \right] \quad (\text{D3})$$

and Γ is the full width at half maximum, the sum of a contribution due to the intrinsic losses along the transmission line and a contribution coming from the nanowire:

$$\Gamma = \Gamma_0 + \Gamma_{\text{NW}} = \frac{4\omega_0}{\pi} \left[\alpha_0 l_0 + \frac{\text{Re}(Z_{\text{NW}})}{Z_0} \right]. \quad (\text{D4})$$

The total internal quality factor of the nanowire resonator can therefore be given as

$$Q_i^{-1} = Q_0^{-1} + Q_{\text{NW}}^{-1} \quad (\text{D5})$$

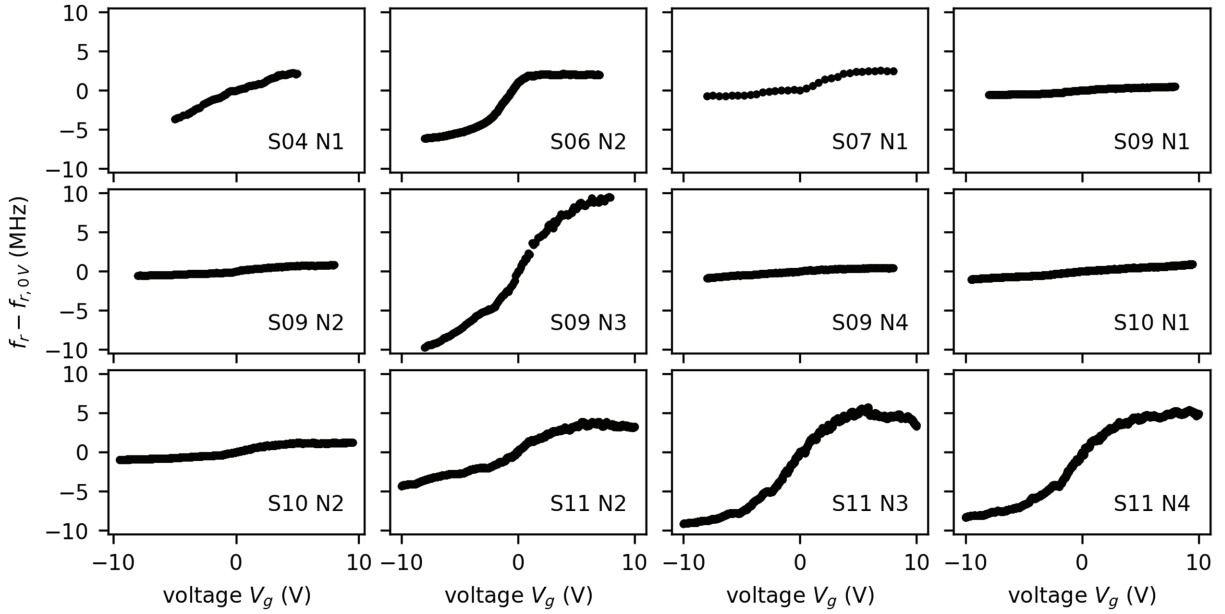


FIG. 6. Frequency shift as a function of gate voltages extracted from fits to S_{21} data for 12 different nanowire resonators. The offset $f_{\text{NW},0\text{V}}$ is listed in Table I.

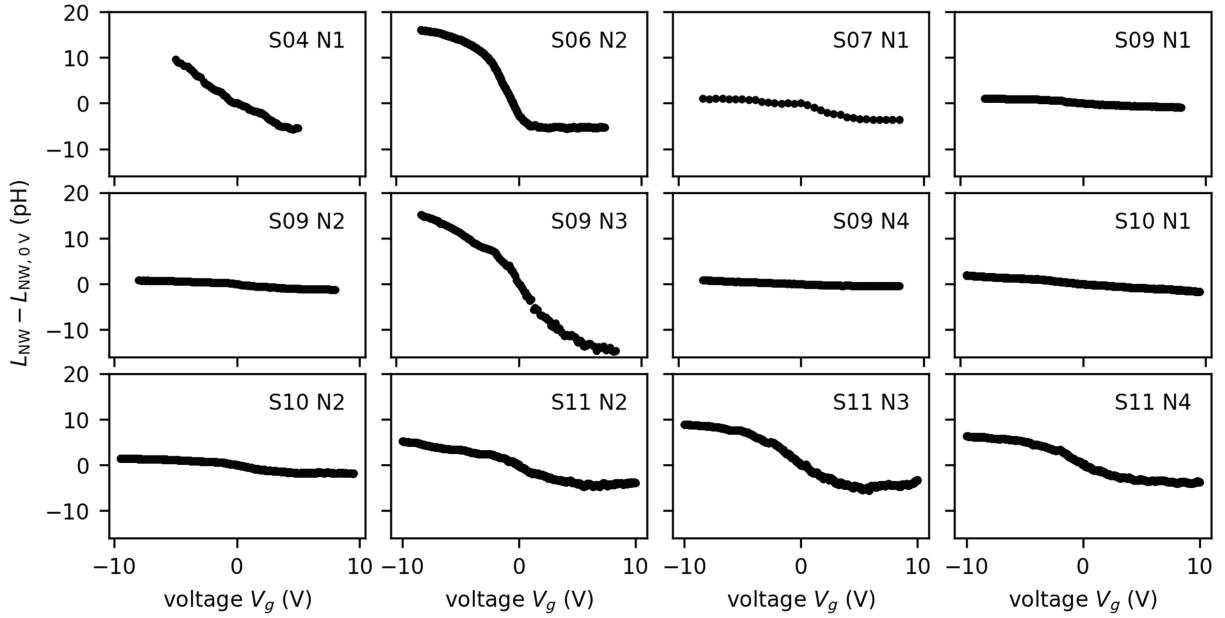


FIG. 7. Change in nanowire inductance as a function of gate voltages for 12 different nanowire resonators. The offset $L_{\text{NW},0V}$ is different for each nanowire and listed in Table I.

with $Q_0 = \omega_0 / \Gamma_0$ and $Q_{\text{NW}} = \omega_0 / \Gamma_{\text{NW}}$. Putting Eqs. (D3) and (D5) together, we obtain the nanowire impedance as a function of the measurable quantities ω_0 , ω_{NW} , Q_i , Q_0 :

$$Z_{\text{NW}} = \frac{\pi Z_0}{4} \left(\frac{1}{Q_i} - \frac{1}{Q_0} \right) + i \frac{\pi Z_0}{2} \frac{\omega_0 - \omega_{\text{NW}}}{\omega_0}. \quad (\text{D6})$$

This number has positive real and imaginary parts for $Q_0 \geq Q_i$ and $\omega_0 \geq \omega_{\text{NW}}$.

APPENDIX E: COMPLEMENTARY MEASUREMENTS

1. Nanowire resonators

During the course of this work, we prepare 11 samples with four nanowire resonators and four reference resonators each. In Table I and Figs. 6 and 7 we report the parameters and basic characterization of all 12 nanowire resonators exhibiting a gate-voltage dependence. Other nanowire resonators are discarded because of shorted gates, highly resistive $\text{Nb}_x\text{Ti}_{1-x}\text{N}$ to nanowire contacts or broken nanowires. The data, which entered the main text, is taken on a single nanowire resonator N2 and reference resonator R1 from sample S11. We consider the data set of S11 as representative for the entire set of measurements.

We design the nanowire resonators starting from the CPW resonators with $Z_0 \gg Z_{\text{NW}}$ by adjusting the geometry, in particular, width w , spacing s , and length l of the CPW transmission line. The resonator parameters are listed in Table I. For all nanowire resonators, the coupling quality factor is $Q_c = 5.5 \times 10^3$. Based on the kinetic

sheet inductance of $\text{Nb}_x\text{Ti}_{1-x}\text{N}$, we calculate the nanowire inductance. We also summarize further key quantities to compare the different nanowires.

In Fig. 6 we compare the gate-voltage dependence of 12 nanowire resonators. We observe a monotonic increase in resonance frequency as a function of gate voltage. The frequency shift is quantified in Table I as Δf_{NW} over a voltage range of ΔV_g . The different magnitudes of the frequency shift in the gate-voltage scan arise from different participation ratios of nanowire to total inductance, but might also be a result of fluctuations between nanowires or due to the orientation of the Al shell relative to the bottom gate, potentially leading to gate screening for unfavorable orientations of the Al shell. We cannot track the position of the Al shell relative to the bottom gate for each nanowire because of top gates encapsulating the nanowire.

The 12 measured nanowires differ in their configuration: they comprise devices with different gate geometries, different nanowire growths, and measurement in different cooldowns. In particular, S04 N1 and S06 N2 use a $2\text{-}\mu\text{m}$ -long nanowire segment with a nanowire diameter of (80 ± 5) nm, and a nominal thickness of the epitaxially grown Al of 6 nm. However, they all exhibit similar gate responses. From this observation, we conclude that the effect of gate-tunable kinetic inductance is reproducible in hybrid superconducting semiconducting nanowires from Al and InAs and not unique to a specific nanowire batch or fabrication process.

Figure 7 shows the decreasing nanowire inductance versus gate voltage for 12 nanowire resonators. The change in inductance is quantified in Table I as ΔL_{NW} . Overall,

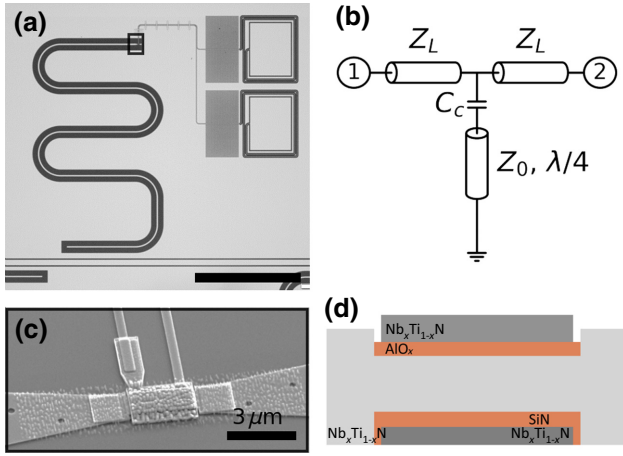


FIG. 8. Measured reference device. (a) Optical image of one quarter-wave coplanar waveguide resonator capacitively coupled to a feedline and shorted to ground via a thick $\text{Nb}_x\text{Ti}_{1-x}\text{N}$ film instead of a proximitized nanowire. Two LC filtered pads left to the resonator connect to the electrostatic gates in the vicinity of the $\text{Nb}_x\text{Ti}_{1-x}\text{N}$ film. (scale bar $300 \mu\text{m}$). (b) Circuit diagram of a measured device. The transmission-line resonator with impedance Z_0 is shunted to ground by a thick $\text{Nb}_x\text{Ti}_{1-x}\text{N}$ film, and capacitively coupled (C_C) to the feedline with characteristic impedance $Z_L = 50 \Omega$. Ports 1 and 2 connect to the external measurement setup. (c) Micrograph of the $\text{Nb}_x\text{Ti}_{1-x}\text{N}$ film, which is galvanically connected to the central conductor of the resonator [black box in (a)]. The $3\text{-}\mu\text{m}$ -long $\text{Nb}_x\text{Ti}_{1-x}\text{N}$ patch is encapsulated by voltage bottom and top gates. Here, neither of the gates is used. (d) Schematic longitudinal cut away of reference structure used for comparison with the nanowire resonator. The nanowire section is replaced by a continuous 150-nm -thick $\text{Nb}_x\text{Ti}_{1-x}\text{N}$ film.

the inductance values are similar within a factor of 2 for most nanowires. The variations between the experiments probably arise from different residual inductances at the $\text{Nb}_x\text{Ti}_{1-x}\text{N}$ to the nanowire interface. These residual inductances do not appear in the reference resonators and thus are specific to the nanowire resonator.

2. Reference resonators

The reference resonator consists of quarter-wave coplanar waveguide resonators capacitively coupled to a feedline and shorted to ground via a thick $\text{Nb}_x\text{Ti}_{1-x}\text{N}$ patch instead of a proximitized nanowire as shown in Fig. 8(a). Two LC filtered pads left to the resonator connect to the electrostatic gates in the vicinity of the $\text{Nb}_x\text{Ti}_{1-x}\text{N}$ patch. However, these gates are not used. The micrograph of the $\text{Nb}_x\text{Ti}_{1-x}\text{N}$ film in Fig. 8(c) shows the $3\text{-}\mu\text{m}$ -long and $1\text{-}\mu\text{m}$ -wide $\text{Nb}_x\text{Ti}_{1-x}\text{N}$ patch encapsulated by voltage bottom and top gates to mimic the same electromagnetic environment as for the nanowire resonator. The cut away in Fig. 8(d) illustrates the difference to the nanowire resonator shown in the main text in Fig. 1(d). This direct comparison

allows us to test the device quality in this multistep fabrication and the superconducting $\text{Nb}_x\text{Ti}_{1-x}\text{N}$ to $\text{Nb}_x\text{Ti}_{1-x}\text{N}$ contact. The reference resonator can be modeled with the equivalent circuit in Fig. 8(b). The transmission-line resonator with characteristic impedance Z_0 identical to the nanowire resonator, but different resonator impedance is capacitively coupled (C_C) to the feedline with characteristic impedance $Z_L = 50 \Omega$. Ports 1 and 2 connect to the external measurement setup.

For the experiment, we design CPW resonators with identical transmission-line impedance as the nanowire resonator, but different length l . The resonator parameters are listed in Table II. We extract the kinetic sheet inductance per square of the $\text{Nb}_x\text{Ti}_{1-x}\text{N}$ film L_k from the reference resonator by comparing the measured resonance frequencies with microwave simulations (AWR Microwave Office) of the full resonator design and numerical calculations based on a conformal mapping technique for CPW transmission lines [46]. We obtain the kinetic sheet inductance from the average over all reference resonators per sample.

3. Geometric inductance of nanowire segment

We estimate the geometric inductance of the nanowire segment using a conformal mapping technique [46]. For a 100-nm -wide and $3\text{-}\mu\text{m}$ -long wire in a CPW geometry with $22\text{-}\mu\text{m}$ spacing to ground, we find a geometric inductance of 4.5 pH . This is about 2% of the total nanowire inductance. This systematic error falls into the uncertainty of the nanowire inductance, thus we neglect the geometric contribution arising from the magnetic self-inductance.

TABLE II. Overview of resonator parameters for all measured reference resonators labeled as sample SX with resonator RY. The designed width w , spacing s , and length l of the CPW resonator as well as the extracted kinetic sheet inductance per square of the $\text{Nb}_x\text{Ti}_{1-x}\text{N}$ film L_k , and the measured resonance frequency f_r are given. In this paper we focus on the reference resonator denoted S11 R1.

Label	w μm	s μm	l μm	L_k $\text{pH}\square^{-1}$	f_r GHz
S04 R1	5	20	2523	5.45	7.423
S04 R2	5	20	2573	5.55	7.239
S06 R1	5	20	2523	5.57	7.372
S06 R2	5	20	2573	5.77	7.155
S07 R1	4	20	4679	5.45	3.798
S09 R1	5	20	4600	7.3	3.704
S09 R2	5	20	2870	7.4	5.910
S10 R1	5	20	4600	7.3	3.709
S10 R2	5	20	2870	7.4	5.918
S11 R1	5	20	4662	5.35	4.042
S11 R2	5	20	4914	5.33	3.838
S11 R3	5	20	2561	5.34	7.360
S11 R4	5	20	2491	5.22	7.616

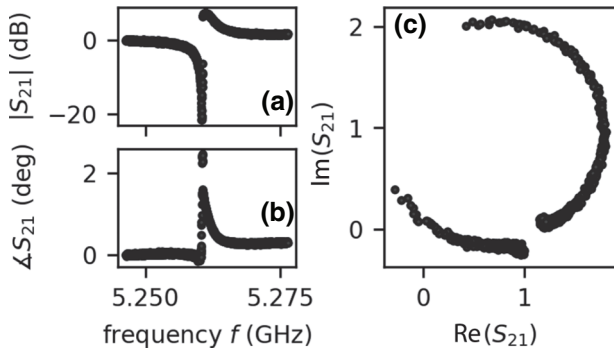


FIG. 9. Scattering parameter S_{21} of bifurcating nanowire resonance in magnitude (a), phase (b) versus frequency and in the complex plane (c) at -113 -dBm input power at the reference plane of the resonator.

4. Resonator bifurcation

Superconducting resonators can exhibit nonlinear behavior, including bifurcation if driven with sufficiently large input power [67]. Figure 9 shows the scattering parameter of a nanowire resonator in magnitude (a), phase (b) versus frequency and in the complex plane (c) at -113 -dBm input power at the reference plane of the resonator. The discontinuity of the circle in Fig. 9c indicates a bifurcation behavior at high readout powers. In the main text we limit our studies to the regime of few intracavity photons

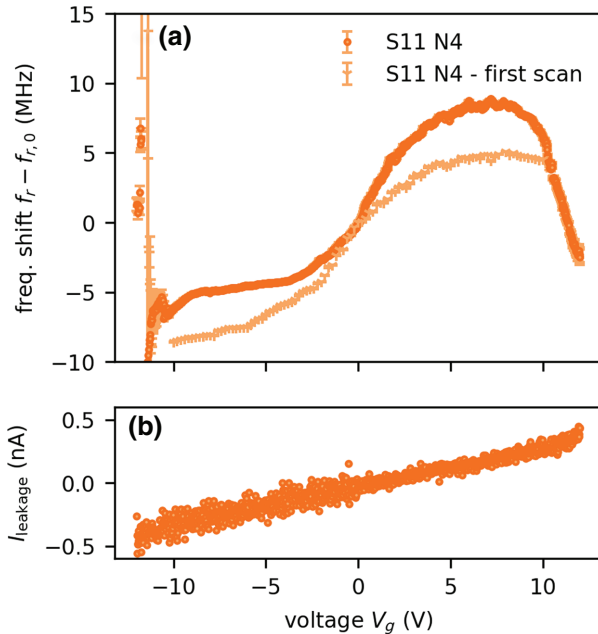


FIG. 10. Gate leakage of nanowire resonator 4. (a) Frequency shift as a function of gate voltages extracted from fits to S_{21} data for resonator S11 N4 in the first scan of the experiment and later after exceeding a gate voltage of $|10$ V|. (b) Leakage current versus gate voltage measured during voltage sweep in the latter case.

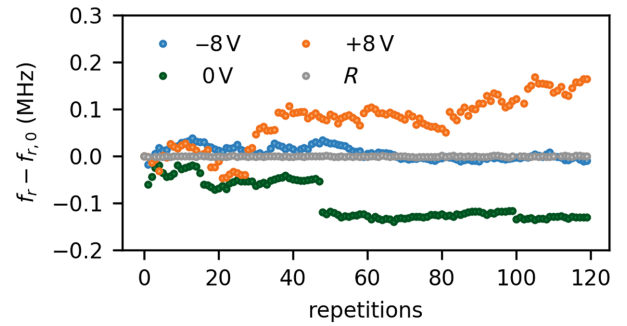


FIG. 11. Gate-voltage stability. Frequency shift of nanowire resonator for three different gate voltages and frequency shift of reference resonator for 120 repetitions with 30-s waiting time between measurement points.

where the signal to noise ratio is sufficient for readout, but where the resonator does not bifurcate.

5. Gate leakage

Figure 10(a) shows the frequency shift of about 13 MHz as a function of gate voltages for nanowire resonator S11 N4 in the first scan of the experiment and after exceeding a gate voltage of $|10$ V| multiple times. Between the two experiments, we observe a different slope around 0 V, but otherwise the same magnitude of the frequency shift.

In Fig. 10(b), while measuring the frequency response of S11 N4 between -12 V and $+12$ V, we record the leakage current through the bottom gate, which increases linearly by about 1 nA. We attribute the sharp drop in internal quality factor [see Fig. 3(a)] at large applied gate voltages to the point where the injection of quasiparticles through the bottom gate reduces the superconducting gap measurably. This is in line with the slightly asymmetric onset in the reduction of the internal quality factor for positive and negative voltages. The data shown in the main text has been taken after exceeding voltages of $|10$ V|. We note however

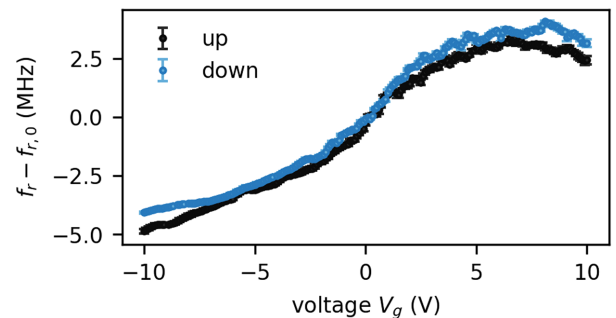


FIG. 12. Gate-voltage hysteresis. Average frequency shift of nanowire resonator over four gate-voltage scans per sweep direction.

that the trends in frequency and internal quality factor versus the control parameters do not seem to be affected in the voltage range from -8 to 8 V.

6. Gate stability and hysteresis

In view of possible applications for frequency-tunable resonators we study the frequency stability over time and the gate hysteresis. Figure 11 shows the frequency shift of the nanowire resonator S11 N2 for three different gate voltages and the frequency shift of the reference resonator S11 R1 for 120 repetitions with 30-s waiting time between measurement points. The reference resonator exhibits a constant frequency in time. Only small variations on the few kHz scale can be observed. The behavior of the nanowire resonator however differs from the reference resonator. For negative gate voltages, the fluctuations in time are on the order of 50 kHz, but the trend is relatively flat otherwise. The more positive we set the gate voltage, the more jumps and drifts appear in the time dependence. We speculate that at this gate voltage sudden reconfigurations of the charge-carrier distribution in the nanowire happen.

Figure 12 shows the average frequency shift of the nanowire resonator for four gate-voltage scans per sweep direction with a reset to zero volt between each scan. The error bar represents the standard deviation and is small compared to the total frequency shift. The size of the error bar is nearly equal over the entire range of gate voltages. We note the offset between the up and down sweeps originating from gate hysteresis or a reconfiguration of the charge-carrier distribution.

-
- [1] R. Meservey and P. M. Tedrow, Measurements of the kinetic inductance of superconducting linear structures, *J. Appl. Phys.* **40**, 2028 (1969).
- [2] A. J. Annunziata, D. F. Santavica, L. Frunzio, G. Catealani, M. J. Rooks, A. Frydman, and D. E. Prober, Tunable superconducting nanoinductors, *Nanotechnology* **21**, 445202 (2010).
- [3] J. Zmuidzinas, Superconducting microresonators: Physics and applications, *Annu. Rev. Condens. Matter Phys.* **3**, 169 (2012).
- [4] N. Samkharadze, A. Bruno, P. Scarlino, G. Zheng, D. P. DiVincenzo, L. DiCarlo, and L. M. K. Vandersypen, High-Kinetic-Inductance Superconducting Nanowire Resonators for Circuit QED in a Magnetic Field, *Phys. Rev. Appl.* **5**, 044004 (2016).
- [5] D. Niepce, J. Burnett, and J. Bylander, High Kinetic Inductance NbN Nanowire Superinductors, *Phys. Rev. Appl.* **11**, 044014 (2019).
- [6] L. Grünhaupt, M. Spiecker, D. Gusenkova, N. Maleeva, S. T. Skacel, I. Takmakov, F. Valenti, P. Winkel, H. Rotzinger, W. Wernsdorfer, A. V. Ustinov, and I. M. Pop, Granular aluminium as a superconducting material for high-impedance quantum circuits, *Nat. Mater.* **18**, 816 (2019).
- [7] P. Kamenov, W.-S. Lu, K. Kalashnikov, T. DiNapoli, M. T. Bell, and M. E. Gershenson, Granular Aluminum Meandered Superinductors for Quantum Circuits, *Phys. Rev. Appl.* **13**, 054051 (2020).
- [8] A. Y. Mironov, D. M. Silevitch, S. V. Postolova, M. V. Burdastyh, T. Proslie, T. I. Baturina, T. F. Rosenbaum, and V. M. Vinokur, Supercapacitance and superinductance of TiN and NbTiN films in the vicinity of superconductor-to-insulator transition, *Sci. Rep.* **11**, 16181 (2021).
- [9] B. A. Mazin, Ph.D. thesis, California Institute of Technology, 2005..
- [10] A. Blais, S. M. Girvin, and W. D. Oliver, Quantum information processing and quantum optics with circuit quantum electrodynamics, *Nat. Phys.* **16**, 247 (2020).
- [11] M. Kjaergaard, M. E. Schwartz, J. Braumüller, P. Krantz, J. I.-J. Wang, S. Gustavsson, and W. D. Oliver, Superconducting qubits: Current state of play, *Annu. Rev. Condens. Matter Phys.* **11**, 369 (2020).
- [12] A. Blais, A. L. Grimsmo, S. M. Girvin, and A. Wallraff, Circuit quantum electrodynamics, *Rev. Mod. Phys.* **93**, 025005 (2021).
- [13] Y.-H. Lin, L. B. Nguyen, N. Grabon, J. San Miguel, N. Pankratova, and V. E. Manucharyan, Demonstration of Protection of a Superconducting Qubit from Energy Decay, *Phys. Rev. Lett.* **120**, 150503 (2018).
- [14] L. B. Nguyen, Y.-H. Lin, A. Somoroff, R. Mencia, N. Grabon, and V. E. Manucharyan, High-Coherence Fluxonium Qubit, *Phys. Rev. X* **9**, 041041 (2019).
- [15] T. M. Hazard, A. Gyenis, A. Di Paolo, A. T. Asfaw, S. A. Lyon, A. Blais, and A. A. Houck, Nanowire Superinductance Fluxonium Qubit, *Phys. Rev. Lett.* **122**, 010504 (2019).
- [16] A. Gyenis, P. S. Mundada, A. Di Paolo, T. M. Hazard, X. You, D. I. Schuster, J. Koch, A. Blais, and A. A. Houck, Experimental Realization of a Protected Superconducting Circuit Derived from the $0-\pi$ Qubit, *PRX Quantum* **2**, 010339 (2021).
- [17] A. Gyenis, A. Di Paolo, J. Koch, A. Blais, A. A. Houck, and D. I. Schuster, Moving Beyond the Transmon: Noise-Protected Superconducting Quantum Circuits, *PRX Quantum* **2**, 030101 (2021).
- [18] H. Zhang, S. Chakram, T. Roy, N. Earnest, Y. Lu, Z. Huang, D. K. Weiss, J. Koch, and D. I. Schuster, Universal Fast-Flux Control of a Coherent, Low-Frequency Qubit, *Phys. Rev. X* **11**, 011010 (2021).
- [19] T. Yamamoto, K. Inomata, M. Watanabe, K. Matsuba, T. Miyazaki, W. D. Oliver, Y. Nakamura, and J. S. Tsai, Flux-driven Josephson parametric amplifier, *Appl. Phys. Lett.* **93**, 042510 (2008).
- [20] P. Krantz, M. Kjaergaard, F. Yan, T. P. Orlando, S. Gustavsson, and W. D. Oliver, A quantum engineer's guide to superconducting qubits, *Appl. Phys. Rev.* **6**, 021318 (2019).
- [21] D. J. Parker, M. Savytskyi, W. Vine, A. Laucht, T. Duty, A. Morello, A. L. Grimsmo, and J. J. Pla, Degenerate Parametric Amplification via Three-Wave Mixing Using Kinetic Inductance, *Phys. Rev. Appl.* **17**, 034064 (2022).
- [22] A. Palacios-Laloy, F. Nguyen, F. Mallet, P. Bertet, D. Vion, and D. Esteve, Tunable resonators for quantum circuits, *J. Low Temp. Phys.* **151**, 1034 (2008).

- [23] O. Naaman, M. O. Abutaleb, C. Kirby, and M. Rennie, On-chip Josephson junction microwave switch, *Appl. Phys. Lett.* **108**, 112601 (2016).
- [24] M. R. Vissers, J. Hubmayr, M. Sandberg, S. Chaudhuri, C. Bockstiegel, and J. Gao, Frequency-tunable superconducting resonators via nonlinear kinetic inductance, *Appl. Phys. Lett.* **107**, 062601 (2015).
- [25] M. Xu, X. Han, W. Fu, C.-L. Zou, and H. X. Tang, Frequency-tunable high- Q superconducting resonators via wireless control of nonlinear kinetic inductance, *Appl. Phys. Lett.* **114**, 192601 (2019).
- [26] S. Mahashabde, E. Otto, D. Montemurro, S. de Graaf, S. Kubatkin, and A. Danilov, Fast Tunable High- Q -Factor Superconducting Microwave Resonators, *Phys. Rev. Appl.* **14**, 044040 (2020).
- [27] G. de Lange, B. van Heck, A. Bruno, D. J. van Woerkom, A. Geresdi, S. R. Plissard, E. P. A. M. Bakkers, A. R. Akhmerov, and L. DiCarlo, Realization of Microwave Quantum Circuits Using Hybrid Superconducting-Semiconducting Nanowire Josephson Elements, *Phys. Rev. Lett.* **115**, 127002 (2015).
- [28] T. W. Larsen, K. D. Petersson, F. Kuemmeth, T. S. Jespersen, P. Krogstrup, J. Nygård, and C. M. Marcus, Semiconductor-Nanowire-Based Superconducting Qubit, *Phys. Rev. Lett.* **115**, 127001 (2015).
- [29] L. Casparis, N. J. Pearson, A. Kringhøj, T. W. Larsen, F. Kuemmeth, J. Nygård, P. Krogstrup, K. D. Petersson, and C. M. Marcus, Voltage-controlled superconducting quantum bus, *Phys. Rev. B* **99**, 085434 (2019).
- [30] M. W. A. de Moor, J. D. S. Bommer, D. Xu, G. W. Winkler, A. E. Antipov, A. Bargerbos, G. Wang, N. van Loo, R. L. M. Op het Veld, S. Gazibegovic, D. Car, J. A. Logan, M. Pendharkar, J. S. Lee, E. P. A. M. Bakkers, C. J. Palmstrøm, R. M. Lutchyn, L. P. Kouwenhoven, and H. Zhang, Electric field tunable superconductor-semiconductor coupling in Majorana nanowires, *New J. Phys.* **20**, 103049 (2018).
- [31] A. E. Antipov, A. Bargerbos, G. W. Winkler, B. Bauer, E. Rossi, and R. M. Lutchyn, Effects of Gate-Induced Electric Fields on Semiconductor Majorana Nanowires, *Phys. Rev. X* **8**, 031041 (2018).
- [32] A. E. G. Mikkelsen, P. Kotetes, P. Krogstrup, and K. Flensberg, Hybridization at Superconductor-Semiconductor Interfaces, *Phys. Rev. X* **8**, 031040 (2018).
- [33] G. W. Winkler, A. E. Antipov, B. van Heck, A. A. Soluyanov, L. I. Glazman, M. Wimmer, and R. M. Lutchyn, Unified numerical approach to topological semiconductor-superconductor heterostructures, *Phys. Rev. B* **99**, 245408 (2019).
- [34] J. G. Kroll, F. Borsoi, K. L. van der Enden, W. Uilhoorn, D. de Jong, M. Quintero-Pérez, D. J. van Woerkom, A. Bruno, S. R. Plissard, D. Car, E. P. A. M. Bakkers, M. C. Cassidy, and L. P. Kouwenhoven, Magnetic-Field-Resilient Superconducting Coplanar-Waveguide Resonators for Hybrid Circuit Quantum Electrodynamics Experiments, *Phys. Rev. Appl.* **11**, 064053 (2019).
- [35] A. Kringhøj, T. W. Larsen, O. Erlandsson, W. Uilhoorn, J. G. Kroll, M. Hesselberg, R. P. G. McNeil, P. Krogstrup, L. Casparis, C. M. Marcus, and K. D. Petersson, Magnetic-Field-Compatible Superconducting Transmon Qubit, *Phys. Rev. Appl.* **15**, 054001 (2021).
- [36] R. M. Lutchyn, E. P. A. M. Bakkers, L. P. Kouwenhoven, P. Krogstrup, C. M. Marcus, and Y. Oreg, Majorana zero modes in superconductor-semiconductor heterostructures, *Nat. Rev. Mater.* **3**, 52 (2018).
- [37] X. Mi, J. V. Cady, D. M. Zajac, J. Stehlik, L. F. Edge, and J. R. Petta, Circuit quantum electrodynamics architecture for gate-defined quantum dots in silicon, *Appl. Phys. Lett.* **110**, 043502 (2017).
- [38] M. S. Khalil, M. J. A. Stoutimore, F. C. Wellstood, and K. D. Osborn, An analysis method for asymmetric resonator transmission applied to superconducting devices, *J. Appl. Phys.* **111**, 054510 (2012).
- [39] S. Probst, F. B. Song, P. A. Bushev, A. V. Ustinov, and M. Weides, Efficient and robust analysis of complex scattering data under noise in microwave resonators, *Rev. Sci. Instrum.* **86**, 024706 (2015).
- [40] A. Bruno, G. de Lange, S. Asaad, K. L. van der Enden, N. K. Langford, and L. DiCarlo, Reducing intrinsic loss in superconducting resonators by surface treatment and deep etching of silicon substrates, *Appl. Phys. Lett.* **106**, 182601 (2015).
- [41] E. A. Tholén, A. Ergül, E. M. Doherty, F. M. Weber, F. Grégis, and D. B. Haviland, Nonlinearities and parametric amplification in superconducting coplanar waveguide resonators, *Appl. Phys. Lett.* **90**, 253509 (2007).
- [42] L. Grünhaupt, N. Maleeva, S. T. Skacel, M. Calvo, F. Levy-Bertrand, A. V. Ustinov, H. Rotzinger, A. Monfardini, G. Catelani, and I. M. Pop, Loss Mechanisms and Quasiparticle Dynamics in Superconducting Microwave Resonators Made of Thin-Film Granular Aluminum, *Phys. Rev. Lett.* **121**, 117001 (2018).
- [43] E. A. Tholén, A. Ergül, K. Stannigel, C. Hutter, and D. B. Haviland, Parametric amplification with weak-link nonlinearity in superconducting microresonators, *Phys. Scr.* **T137**, 014019 (2009).
- [44] R. Vijay, M. H. Devoret, and I. Siddiqi, Invited Review Article: The Josephson bifurcation amplifier, *Rev. Sci. Instrum.* **80**, 111101 (2009).
- [45] C. K. Andersen, A. Kamal, N. A. Masluk, I. M. Pop, A. Blais, and M. H. Devoret, Quantum Versus Classical Switching Dynamics of Driven Dissipative Kerr Resonators, *Phys. Rev. Appl.* **13**, 044017 (2020).
- [46] R. Simons, *Coplanar Waveguide Circuits, Components, and Systems* (John Wiley & Sons, Ltd, New York, 2001), Chap. 8, pp. 203–236.
- [47] D. C. Mattis and J. Bardeen, Theory of the anomalous skin effect in normal and superconducting metals, *Phys. Rev.* **111**, 412 (1958).
- [48] M. Tinkham, *Introduction to Superconductivity* (Dover Publications, New York, 2004).
- [49] J. Shen, G. W. Winkler, F. Borsoi, S. Heedt, V. Levajac, J.-Y. Wang, D. van Driel, D. Bouman, S. Gazibegovic, R. L. M. Op Het Veld, D. Car, J. A. Logan, M. Pendharkar, C. J. Palmstrøm, E. P. A. M. Bakkers, L. P. Kouwenhoven, and B. van Heck, Full parity phase diagram of a proximitized nanowire island, *Phys. Rev. B* **104**, 045422 (2021).
- [50] D. Phan, J. Senior, A. Ghazaryan, M. Hatefipour, W. M. Strickland, J. Shabani, M. Serbyn, and A. P. Higginbotham, Detecting Induced $p \pm ip$ Pairing at the Al-InAs Interface with a Quantum Microwave Circuit, *Phys. Rev. Lett.* **128**, 107701 (2022).

- [51] T. Kiendl, F. von Oppen, and P. W. Brouwer, Proximity-induced gap in nanowires with a thin superconducting shell, *Phys. Rev. B* **100**, 035426 (2019).
- [52] C. Reeg, D. Loss, and J. Klinovaja, Finite-size effects in a nanowire strongly coupled to a thin superconducting shell, *Phys. Rev. B* **96**, 125426 (2017).
- [53] C. Reeg, D. Loss, and J. Klinovaja, Metallization of a Rashba wire by a superconducting layer in the strong-proximity regime, *Phys. Rev. B* **97**, 165425 (2018).
- [54] B. D. Woods, T. D. Stanescu, and S. Das Sarma, Effective theory approach to the Schrödinger–Poisson problem in semiconductor Majorana devices, *Phys. Rev. B* **98**, 035428 (2018).
- [55] G. C. Ménard, F. K. Malinowski, D. Puglia, D. I. Pikulin, T. Karzig, B. Bauer, P. Krogstrup, and C. M. Marcus, Suppressing quasiparticle poisoning with a voltage-controlled filter, *Phys. Rev. B* **100**, 165307 (2019).
- [56] V. Mourik, K. Zuo, S. M. Frolov, S. R. Plissard, E. P. A. M. Bakkers, and L. P. Kouwenhoven, Signatures of Majorana fermions in hybrid superconductor-semiconductor nanowire devices, *Science* **336**, 1003 (2012).
- [57] Ö. Gül, D. J. van Woerkom, I. van Weperen, D. Car, S. R. Plissard, E. P. A. M. Bakkers, and L. P. Kouwenhoven, Towards high mobility InSb nanowire devices, *Nanotechnology* **26**, 215202 (2015).
- [58] I. van Weperen, B. Tarasinski, D. Eeltink, V. S. Pribiag, S. R. Plissard, E. P. A. M. Bakkers, L. P. Kouwenhoven, and M. Wimmer, Spin-orbit interaction in InSb nanowires, *Phys. Rev. B* **91**, 201413(R) (2015).
- [59] S. M. Albrecht, A. P. Higginbotham, M. Madsen, F. Kuemmeth, T. S. Jespersen, J. Nygård, P. Krogstrup, and C. M. Marcus, Exponential protection of zero modes in Majorana islands, *Nature* **531**, 206 (2016).
- [60] F. K. Malinowski, L. Han, D. de Jong, J.-Y. Wang, C. G. Prosko, G. Badawy, S. Gazibegovic, Y. Liu, P. Krogstrup, E. P. A. M. Bakkers, L. P. Kouwenhoven, and J. V. Koski, Radio-frequency C-V measurements with sub-attofarad sensitivity, [arXiv:2110.03257](https://arxiv.org/abs/2110.03257) (2021).
- [61] S. Ahn, H. Pan, B. Woods, T. D. Stanescu, and S. Das Sarma, Estimating disorder and its adverse effects in semiconductor Majorana nanowires, *Phys. Rev. Mater.* **5**, 124602 (2021).
- [62] W. Wustmann and V. Shumeiko, Parametric resonance in tunable superconducting cavities, *Phys. Rev. B* **87**, 184501 (2013).
- [63] L. J. Splitthoff, A. Bargerbos, L. Grünhaupt, M. Pita-Vidal, J. J. Westorp, Y. Liu, A. Kou, C. K. Andersen, and B. van Heck, Gate-tunable kinetic inductance in proximitized nanowires: Data and Code (2022).
- [64] P. Krogstrup, N. L. B. Ziino, W. Chang, S. Albrecht, M. H. Madsen, E. Johnson, J. Nygård, C. M. Marcus, and T. S. Jespersen, Epitaxy of semiconductor-superconductor nanowires, *Nat. Mater.* **14**, 400 (2015).
- [65] D. Flanigan, Resonator fitter, GitHub repository (2021), 2ef16c41558184ce54069f27a734e382bb0c5067, <https://github.com/danielflanigan/resonator.git>.
- [66] D. M. Pozar, *Microwave Engineering* (Wiley, Hoboken, NJ, 2012), 4th ed.
- [67] L. J. Swenson, P. K. Day, B. H. Eom, H. G. Leduc, N. Llombart, C. M. McKenney, O. Noroozian, and J. Zmuidzinas, Operation of a titanium nitride superconducting microresonator detector in the nonlinear regime, *J. Appl. Phys.* **113**, 104501 (2013).